Materials and Design 167 (2019) 107647

Contents lists available at ScienceDirect

Materials and Design

journal homepage: www.elsevier.com/locate/matdes

Achieving self-enhanced thermal barrier performance through a novel hybrid-layered coating design

Guang-Rong Li [a], Li-Shuang Wang [b], Guan-Jun Yang [a,*]

[a] State Key Laboratory for Mechanical Behavior of Materials, School of Materials Science and Engineering, Xi'an Jiaotong University, Xi'an 710049, China
[b] School of Materials Science and Engineering, Xi'an Shiyou University, Xi'an 710065, China

HIGHLIGHTS

- A novel hybrid-layered TBC was prepared by alternate stacking of dense splats and porous nanoheaps.
- Degree of degradation in thermal conductivity decreases from 80% to 100% for conventional coatings to ~20% for novel coatings.
- Nearly 50% thermal barrier performance is self-enhanced during thermal exposure.

GRAPHICAL ABSTRACT

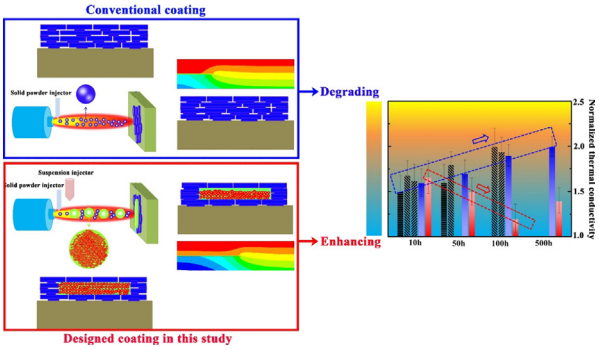

ARTICLE INFO

Article history:
Received 30 October 2018
Received in revised form 10 January 2019
Accepted 8 February 2019
Available online 10 February 2019

Keywords:
Thermal barrier coatings
Sintering
Structure design
Degradation-resistance
Self-enhancing

ABSTRACT

The thermal insulation and durability of thermal barrier coatings (TBCs) are mainly affected by sintering-induced healing of 2D micropores, which is inevitable under high temperature conditions. In this study, we designed and prepared novel hybrid-layered TBCs. During thermal exposure, the degree of degradation in thermal conductivity is observed to decrease from 80 to 100% for conventional coatings to ~20% for the novel coatings. For a detailed understanding, the evolution of the hybrid-layered TBCs can be divided into two stages: during stage I (0—10 h), ultrafast healing of 2D micropores occurs, mainly caused by the multiple contacts between the counter-surface. At this stage, the thermal and mechanical properties also increase sharply. During stage II (after 10 h), some new 2D mesopores are formed. Compared with the 2D micropores, the newly formed 2D mesopores have a much larger aspect ratio that increases the ratio of the effective area for thermal insulation from 10 to 30% to 60%, which accounts for the ~50% self-enhancement in the thermal barrier performance. This self-enhancing behavior is expected to prolong the lifetime and increase the performance of the TBCs, which is the main objective of using advanced TBCs in next-generation applications.

1. Introduction

Thermal barrier coatings (TBCs) are used to protect metallic components against heat flux in aircraft engines and land-based gas turbines. Application of TBCs enables the engines to operate at higher temperatures, thus improving their overall efficiency. In addition, the TBC decreases the temperature experienced by the coated components,

* Corresponding author at: State Key Laboratory for Mechanical Behavior of Materials, School of Materials Science and Engineering, Xi'an Jiaotong University, Xi'an, Shaanxi 710049, China.
E-mail address: ygj@mail.xjtu.edu.cn (G.-J. Yang).

https://doi.org/10.1016/j.matdes.2019.107647

Table 1
Thermal and mechanical properties of the YSZ bulk materials and coatings before and after thermal exposure.

Properties	As-deposited YSZ coatings (average value)	YSZ coatings after thermal exposure (average value)	Bulk YSZ
Thermal conductivity ($W \cdot m^{-1} \cdot K^{-1}$)	1 [23,24]	1.8 [23,25,31–36]	2.5 [28,29]
Elastic modulus (GPa)	20 [25–27]	60 [27,37–40]	210 [29,30]

thereby extending their lifetime. Therefore, TBCs have been playing a crucial role in the development of engines since the past few decades [1–6]. Commonly, a TBC is formed by two layers: a ceramic layer (called the top coat) applied on the exterior to insulate against the heat flux, and a metallic layer (called the bond coat) deposited between the top coat and the underlying substrate [7–9]. Nowadays, however, advanced engines often require TBCs to be characterized by high thermal insulation and a long lifetime; and hence, these are the key requirements for advanced TBCs in future applications [10–12].

The challenge is to retain high performance despite the significant changes in the ceramic structure caused by sintering during thermal exposure. Plasma spraying is often used to prepare the top coat in land-based gas turbines [13–18]. The plasma-sprayed (PS) top coat exhibits a lamellar structure with connected inter- and intra-splat pore networks [19,20], which can also be observed in other thermally sprayed coatings [21,22]. Due to this unique porous microstructure, the TBCs exhibit very low thermal conductivities and high strain tolerance at their as-deposited states. For example, PS yttria-stabilized zirconia (PS-YSZ) has a through-thickness thermal conductivity of approximately 1 $W \cdot m^{-1} \cdot K^{-1}$ [23,24], and in-plane elastic modulus of approximately 30 GPa [25–27]. The thermal and mechanical properties of the PS top coat are at least 40% lower with respect to those of the bulk YSZ [28–30]; however, since sintering of ceramic coatings occurs during thermal exposure, the thermal conductivity can be increased by approximately 80% [23,25,31–36], and the in-plane elastic modulus can be increased by approximately 200% [27,37–40]. Table 1 shows the thermal and mechanical properties of the YSZ bulk materials and coatings before and after thermal exposure. This suggests that the initial coatings with high performances are significantly degraded when exposed to high temperatures. Moreover, it is reported that the degradation occurs mostly during the initial stage of the exposure; for example, in the case of thermal exposure at 1300 °C for 500 h, approximately 80% of the total increment in the elastic modulus is completed during the initial 10 h [41]. Since degradation tremendously threatens the lifetime as well as the thermal insulative function of the TBCs, there is an urgent need for designing a TBC structure capable of degradation-resistant behavior [42].

Since thermal exposure is inevitable for the TBCs, their structure design should take into consideration the sintering effect. In conventional PS-TBCs, sintering-induced degradation is highly associated with the contraction of the ceramic top coat. In fact, the contraction is a result of the healing of the inter-splat pores and intra-splat cracks (called 2D micropores), which can be observed with a transmission electron microscope [43]. Statistical data also suggest that the healing of the 2D micropores dominates the structural changes during the sintering [44,45]. Therefore, the key to designing a degradation-resistant structure is to form new pores that counteract the loss of the 2D micropores. The method used for anode loss protection against corrosion was the source of inspiration for the structural design used in this study [46–48]; following is a detailed explanation of the design: a conventional PS-TBC is mainly stacked by single-type layers called dense splats. During thermal exposure, the lamellar zone is significantly contracted. However, if porous splats are embedded into the conventional dense splats, the differential contraction behaviors of these two types of splats would lead to an interfacial opening that appears in the form of a pore. Thus, a hybrid-layered structure could be an effective solution for the sintering-induced degradation.

In this study, a hybrid-layered TBC was designed and prepared using a co-spraying process; and the changes in the structure and properties during thermal exposure were investigated to analyze the degradation-resistant behavior. A structural model was used to correlate the structure and properties; and the mechanisms of the newly formed pores and their effect to counteract degradation were discussed. This novel hybrid-layered structure is expected to help in the designing of advanced TBCs.

2. Experimental procedure

2.1. Structural design and sample preparation

Thermal insulation performance is primarily determined by the pore orientation; and it is reported that the pores perpendicular to the

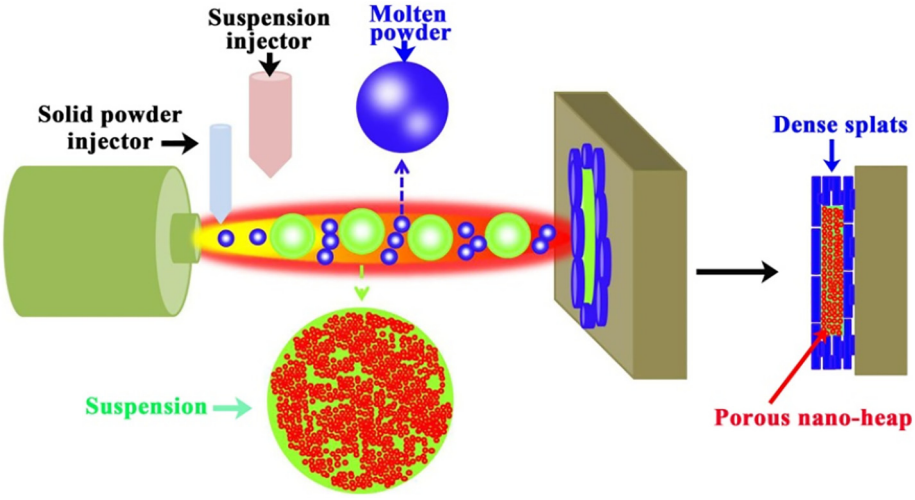

Fig. 1. Schematic of the preparation of the hybrid-layered coatings.

Table 2
Parameters of the plasma spraying and suspension plasma spraying.

Parameters	Plasma spraying	Suspension plasma spraying
Plasma arc voltage, V	70	65
Plasma arc current, A	600	600
Flow rate of primary gas (Ar), L/min	50	60
Flow rate of secondary gas (H_2), L/min	7	4
Flow rate of powder feeding gas (N_2), L/min	4.5	4.5
Liquid flow rate, mL/min	/	20
Spray distance, mm	80	250
Torch traverse speed, mm/s	500	2000

heat flux would maximize the thermal barrier performance [28,49]. Therefore, the morphology of the embedded zone should be consistent with that of the splat-stacking zone. In this way, the interfacial openings or pores can be oriented in a direction perpendicular to the heat flux. The hybrid-layered structure designed in this study is shown in Fig. 1. The following are the features of the hybrid-layered coatings: (i) the coating is formed by the alternate stacking of dense splats and porous splats; (ii) the term dense splats refers to the conventional splats resulting from the resolidified powders during plasma spraying; (iii) the porous splats are the nanoparticle heaps, referred to as the nanoheaps; and (iv) a nanoheap is surrounded by the dense splats to realize the structural integrity.

The hybrid-layered coating was deposited by a plasma co-spraying method: commercially available hollow spherical powders (−75 to +45 μm, Metco 204B-NS, Sulzer Metco Inc., New York, USA) were used to deposit the dense splats, whereas a nanoparticle suspension was used to form the nanoheaps. The 8YSZ suspension was obtained by mixing nanostructured ZrO_2 (1–20 nm) and Yttrium (III) nitrate hexahydrate with deionized water. A water-based suspension UG-R10W (36 wt% of nanostructured ZrO_2 in deionized water) and yttrium (III) nitrate hexahydrate were selected to form a suspension with a mass ratio of 0.0533. A schematic of the co-spraying setup can be seen in Fig. 1. A commercial plasma spraying system (GP-80, 80 kW class, Jiujiang, China) equipped with a suspension injector was used to deposit the hybrid-layered coatings. The suspension injector has an internal diameter of 0.2 mm. It is worth noting that the spraying distance of the suspension should be controlled to retain the original nanoparticles upon stacking on the coating. In this study, disk-shaped nanoheaps are required, which can retain the nanocharacteristics of the original powders and form new pores in a direction perpendicular to the heat flux. Increasing the spray distance would be an effective method to obtain the disk-shaped nanoheaps. In our previous report [50], the optimized distance between the torch and the suspension injector was 20 mm, and the distance between the suspension injector and substrate was 250 mm. Thus, disk-shaped nanoheaps with a diameter of ~150 μm were obtained. To avoid overlap, a very high torch traverse speed (2000 mm/s) was selected for the deposition of suspension. Moreover, to retain the stability of the suspensions, magnetic stirring was used during the entire process of suspension preparation and spraying. The solid and suspension spray parameters are listed in Table 2.

The solid powders and suspension were alternately sprayed on a stainless steel substrate (φ12.7 mm × 4 mm) for the sample preparation; the following is a description of the process: (i) the solid powders were deposited to a thickness of ~10 μm, with each splat 1–2 μm thick; (ii) subsequently, several nanopowder heaps were deposited on the predeposited coating in step (i); each heap had a thickness of approximately 2–4 μm; (iii) steps (i) and (ii) were repeated until the total thickness was 1 mm. In the hybrid-layered coatings, most regions were deposited using a conventional plasma spray procedure. Thus, mass production in industrial applications is possible to be realized using this method. For comparison, conventional coatings were also deposited using pure solid powders having the same parameters as shown in Table 2. In addition to the disk-shaped samples (φ12.7 mm × 4 mm), some rectangular samples (60 mm × 10 mm × 1 mm) were prepared for the measurement of the macroscopic properties.

Before thermal exposure, the substrate was removed with a hydrochloric acid solution to obtain free-standing samples. Subsequently, the samples were isothermally heated to a temperature of 1300 °C in a furnace. After different durations, the samples were allowed to cool to room temperature. During the heating up process, the heating rate was fixed at 20 °C/min from room temperature to 1300 °C; and after the thermal exposure, the samples were cooled at a rate of 10 °C/min.

2.2. Microstructural characterization and measurement of properties

The morphology of the coatings was observed by scanning electron microscopy (SEM) (TESCAN MIRA3, Brno, Czech Republic). The length and width of 2D pores were determined from 50 SEM images at 5000× magnification, as shown in Fig. 2. Subsequently, the length density (defined as the total length of all pores per unit area) and aspect ratio (defined as the ratio of the length to width of a pore) were calculated; more details on the length measurement can be found elsewhere [44]. In-situ observation of pore healing was conducted by SEM; the detailed procedure described elsewhere [41] is briefly presented herein as follows: (i) a target pore is found from the cross-section of the samples at high magnification (e.g., 50,000×); (ii) the magnification is gradually decreased to observe the macroscopic morphology of the sample; (iii) the target position is fixed by the corresponding coordinates; and (iv) after thermal exposure, the target is relocated according to its coordinates. In addition, high-resolution transmission electron microscopy (HRTEM, JEM-2100F, JEOL, Japan) was used to observe the pore-healing behavior. The roughening behavior of the pore surface was characterized by atomic force microscopy (AFM, Asylum Research Cypher, USA).

As the mechanical properties of the PS-TBCs often appear to be scale-sensitive [51], multi-scale properties are determined in this study. The microscale elastic modulus was determined by a Knoop indentation test (Buehler Micromet 5104, Akashi Corporation, Japan) using the disk-shaped samples (φ12.7 mm × 1 mm). The macroscopic elastic modulus was measured via a three-point bending test (Instron 5943, USA) using rectangular samples (60 mm × 10 mm × 1 mm). Given the fact that the strain is often generated along the coating surface

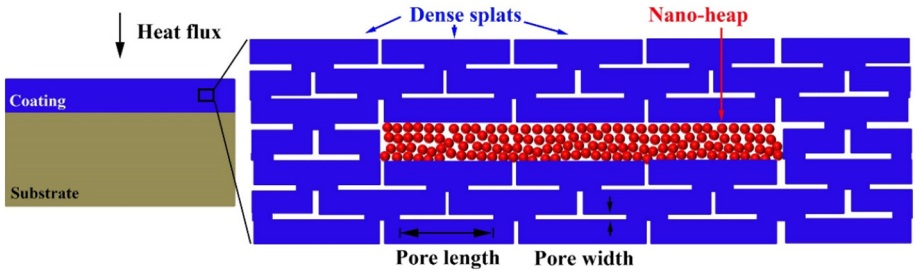

Fig. 2. Schematic of the orientation and dimensions of the 2D pores.

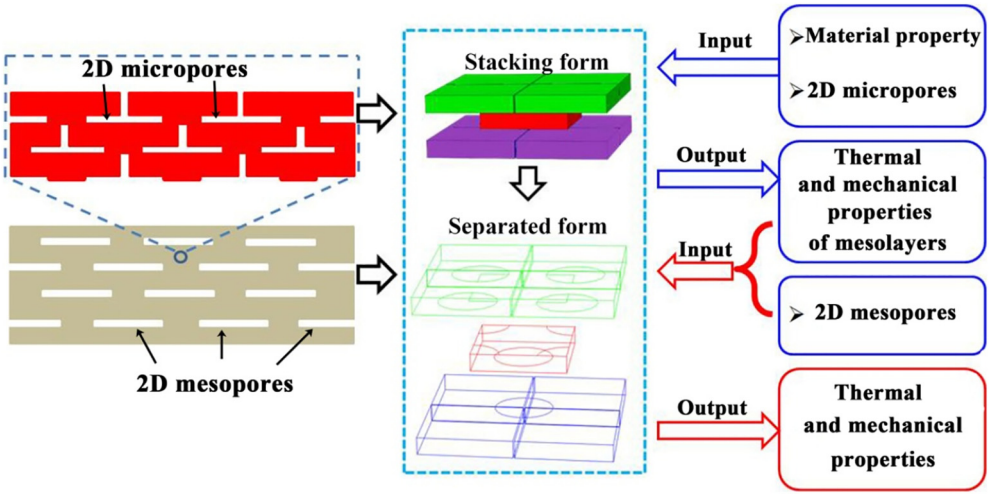

Fig. 3. Model development for the multi-scale property prediction.

[52], only the in-plane elastic moduli were determined. During the test, the elastic modulus can be obtained by the following formulas:

$$w = \frac{PL^3}{48D} \tag{1}$$

$$D = \frac{Eh^3}{12(1-\nu^2)} \tag{2}$$

where P is the load applied at the center of the span, L is the span between the two supports, D is the bending stiffness, w is the central deflection, E is the elastic modulus of the coating, h is the coating thickness, and ν is the Poisson's ratio of the coating.

The thermal conductivity of the samples was determined via a laser flash method using disk-shaped samples (φ12.7 mm × 1 mm) and the following equation [15,53]:

$$\lambda = \rho \cdot C_P \cdot \alpha \tag{3}$$

where λ is the calculated thermal conductivity, ρ is the density, C_P is the heat capacity, and α is the thermal diffusivity.

The thermal diffusivity was measured using a laser flash analyzer (Netzsch, Germany), and at least three samples were used to minimize errors. The value of C_P was determined by differential scanning calorimetry (DSC 404, Netzsch, Germany), while the value of ρ was obtained by dividing the mass of the sample by its volume.

2.3. Prediction of properties

A structural model was developed to predict the thermal and mechanical properties affected by the changes in the 2D pore density, as shown in Fig. 3. Based on the sample preparation procedure described in Section 2.1, the 10 μm thick layers (called meso-layers) are actually formed by the stacking of micro-layers, each having a thickness of 1–2 μm. Therefore, inside the meso-layers, there are some micro-layers formed by dense splats. During the deposition of the micro-layers, the layers are partially bonded, leading to the formation of inter-splat pores. In addition, some intra-splat cracks are formed to release the quenching stress; this is very common in PS ceramic coatings [19,24,54]. Therefore, there are some 2D micropores between the micro-layers. The input data for the prediction are the changes in the length density of the 2D pores, and the assumptions made for the model are described as follows: (i) the micro- and meso-layers are formed by micro- and meso-structural units, respectively (the dimensions of the structural units can be found in Table 3); (ii) the circular bonding areas between the layers are located at the bottom of the center of the upper layers; and (iii) the stacking of the micro- and meso-structural units is uniform. This means that the circular bonding area of every structural unit is exactly and equably located at the four corners of the four structural units in the lower layer, as shown in the "separated form" in Fig. 3. To eliminate the dimensional effect of the structure, a periodic pattern was used by applying proper periodic boundary conditions on the corresponding pair surfaces. The details of the periodic boundary conditions can be found elsewhere [55]. The structural parameters, including the length and thickness of the splats, are obtained from the statistical data on the coatings, while intrinsic material parameters are determined from other references or experiments [54], as shown in Table 3. The properties of the micro-layers of the hybrid-layered structure were calculated first. Subsequently, these values were used as input parameters to calculate the properties of the meso-layers. The x-z plane refers to the reference plane (in-plane direction), which is vertical to the heat flux.

The in-plane elastic modulus was predicted by the following method: (i) a tensile strain (0.1%) perpendicular to the heat flux was applied to the cross-section of the periodic pattern; (ii) the reaction force on the cross-section was obtained; and (iii) the elastic modulus was determined from the stress–strain curve.

The thermal conductivity was predicted using a commercially available ANSYS software (afflicted with ANSYS finite element code APDL). The PLANE55 element (four nodes element, axisymmetric ring) were used in the model. Heat transfer in a porous structure generally occurs in three ways: conduction, convection, and radiation; and the Grashof number (G_r) is used to explain the convective effect in closed pores:

$$G_r \approx \frac{g\Delta T {d_v}^3 {\rho_d}^2}{T\eta^2} \tag{4}$$

Table 3
Structural and intrinsic parameters used as the input data.

Parameters	Values
Thermal conductivity of bulk YSZ, $W\cdot m^{-1}\cdot K^{-1}$	2.5
Thermal conductivity of pores, $W\cdot m^{-1}\cdot K^{-1}$	0.025
Young's modulus of bulk YSZ, GPa	205
Poisson's ratio	0.23
Mean length of a micro-structural unit, μm	10
Mean thickness of a micro-structural unit, μm	1
Mean thickness of a meso-structural unit, μm	8

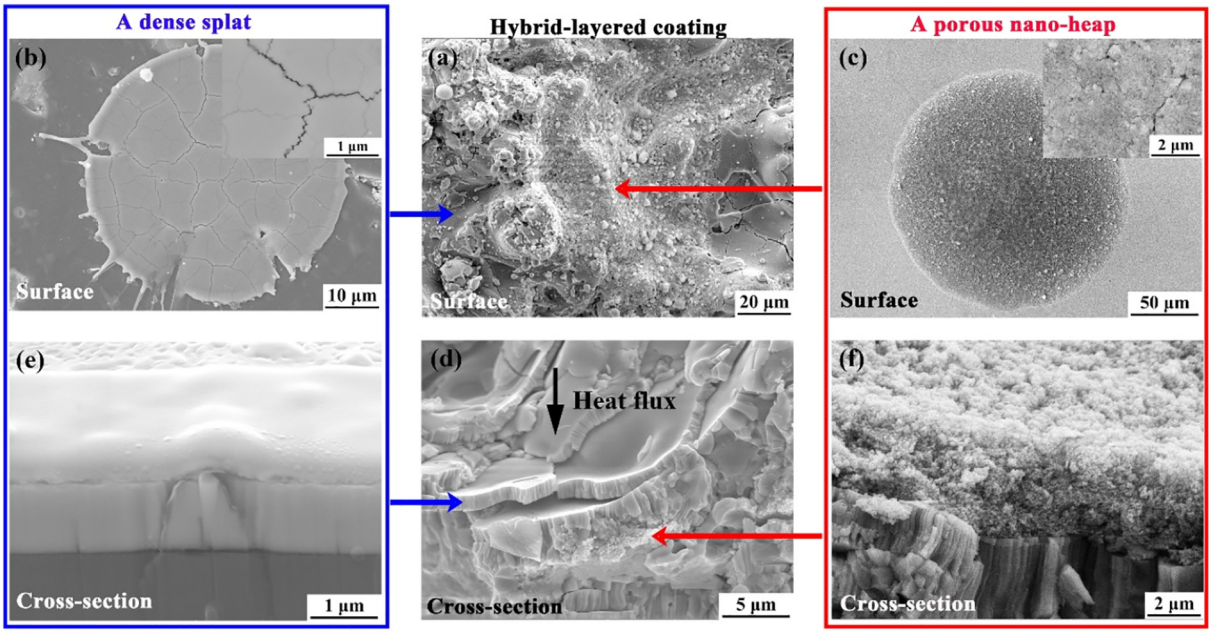

Fig. 4. Morphology of the hybrid-layered coating at as-deposited state: (a) surface morphology of the coating, (b) and (c) are the surface morphologies of a dense splat and a porous nanoheap, respectively; (d) cross-section of the coating; and (e) and (f) are the cross-sections of a dense splat and a porous nanoheap, respectively.

where g is the gravitational acceleration, ρ_d and η are the density and (dynamic) viscosity of the gas, respectively; T is the surrounding temperature, ΔT is the difference in temperature within the pore, and d_v is the characteristic size of a pore.

If G_r is larger than 1000, the convective effect is non-negligible. Given the reasonable variables of TBCs (i.e., ρ_d is 1 kg·m^{-3}, P is 1–40 bar, T is 293.15–1773.15 K, ΔT is 10 K, and $d_v < 1$ mm), the resulting G_r is significantly smaller than 1000. Therefore, it is reasonable to ignore the convective effect inside the TBCs.

Although radiation could be non-negligible at high temperatures, this study focuses on the effect of microstructure on the heat flux. Hence, for the purpose simplification, heat transfer by radiation was neglected. Therefore, only conduction was considered for the investigation of the heat transfer in this study.

Since the heat flux from the top to the bottom of the model should be equal to the heat exchange between the bottom and the environment, adiabatic boundary conditions were applied to the pair-surfaces of the left and right sides. Based on Fourier's law of heat conduction, the heat flux transferred into the structure from the top surface, q_{in}, is given by Eq. (5):

$$q_{in} = \frac{k_e(T_D - T_T)}{H} \tag{5}$$

Correspondingly, the heat flux transferred out of the structure at the bottom surface, q_{out}, is given by Eq. (6):

$$q_{out} = h(T_T - T_S) \tag{6}$$

Based on the principle of energy conservation, the following relationship is obtained:

$$q_{in} = -q_{out} \tag{7}$$

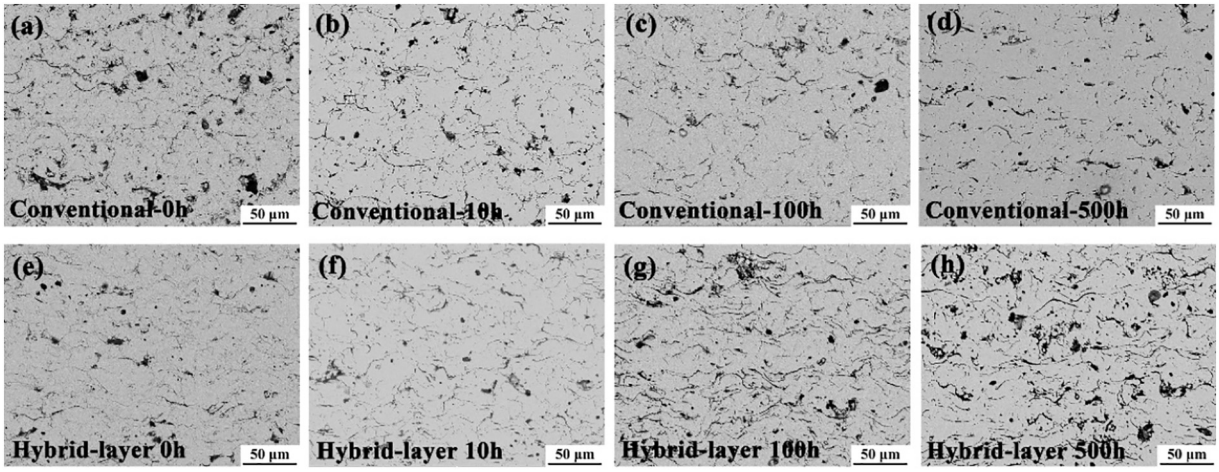

Fig. 5. Evolution of the microstructures during thermal exposure: (a)–(d) are the conventional coatings exposed for different time, and (e)–(f) are the hybrid-layered coatings with different exposure durations.

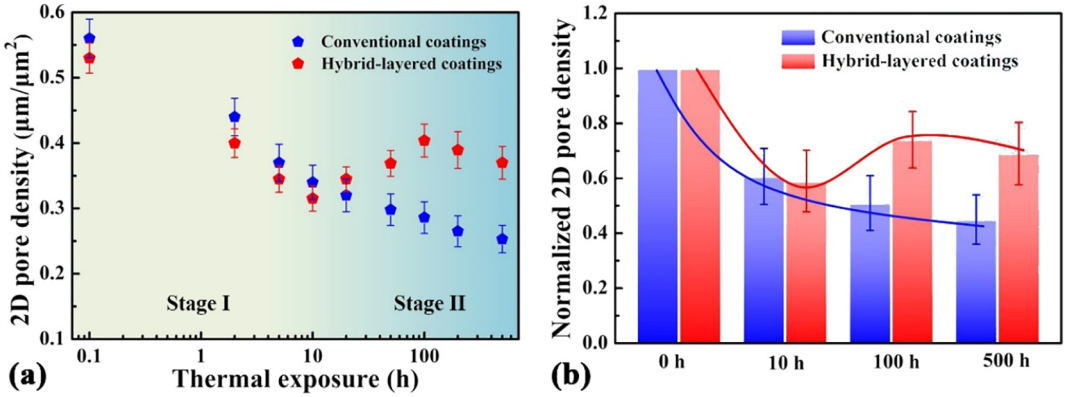

Fig. 6. Changes in 2D pore density during thermal exposure: (a) 2D pore density as a function of duration, and (b) normalized 2D pore density at different durations.

Therefore, the effective thermal conductivity of the structure k_e is given by Eq. (8):

$$k_e \approx \frac{(T_D - T_S)hH}{\Delta T'} \tag{8}$$

where T_D is the top surface temperature of the top coat, T_S is the environmental temperature, h is the thermal convection coefficient, H is the height of model, and $\Delta T'$ is the temperature difference between the top and the bottom surfaces.

3. Results

3.1. Evolution of microstructure during thermal exposure

Fig. 4 shows the morphology of the as-sprayed coatings. It is observed that the hybrid-layered coating is formed by the alternate stacking of the dense splats and porous nanoheaps. The dense splats are observed to be composed of columnar grains. Some 2D micropores can be clearly observed in the layer structure, which is consistent with the previous reports [16,24]. The nanoheaps appear to be disk-shaped and oriented perpendicular to the heat flux. This special orientation would be effective in thermal insulation.

Fig. 5 shows the evolution of the microstructure during thermal exposure. During the initial short thermal exposure, the evolution of the hybrid-layered coatings is observed to be similar to that of the conventional ones, and the 2D micropores are significantly healed. However, during the subsequent long thermal exposure, differential evolutions are observed between these two types of coatings: the hybrid-layered coatings appear to have much more pores than the conventional coatings. While in the conventional coatings, the average length of the micropores is approximately10 μm, in the hybrid-layered coatings, it is approximately 50 μm; hence, they are called 2D mesopores.

Fig. 6 displays the changes in 2D pore density as a function of the duration of the thermal exposure. The entire evolution process can be divided into two stages: during stage I, the density of the 2D pores decreases at a high rate, irrespective of the type of coating. During stage II, however, the decrease in the density of the 2D pores continues in the conventional coatings although at a much slower rate, while the 2D pore density increases in the hybrid-layered coatings. In brief, the structural evolution suggests that some new 2D pores are spontaneously formed in the hybrid-layered structure, which is due to the sintering that occurs during thermal exposure.

3.2. Changes in thermal and mechanical properties during thermal exposure

Fig. 7 shows the changes in the thermal and mechanical properties during thermal exposure. In case of the mechanical properties, it is observed that the macroscopic elastic modulus is significantly lower than the microscopic elastic modulus. This is due to the scale-sensitive features of the PS ceramic coatings [41]. After thermal exposure for 500 h, the increment in the microscopic elastic modulus of the hybrid-layered coatings is approximately 70%, which is lower than that of the conventional coatings (approximately 120%). The increase rate during stage I is approximately 2.7 GPa/h, while it is 0.02 GPa/h during stage II. Moreover, a slight decrease in the macroscopic elastic modulus of the hybrid-layered coatings is observed during stage II. In the case of thermal properties, an obvious decrease in the thermal conductivity of

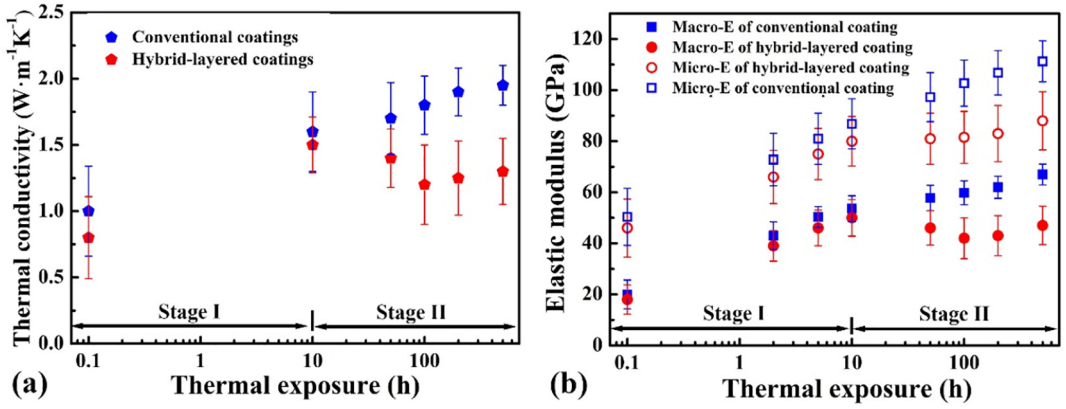

Fig. 7. Changes in properties during thermal exposure: (a) thermal conductivity, and (b) elastic modulus.

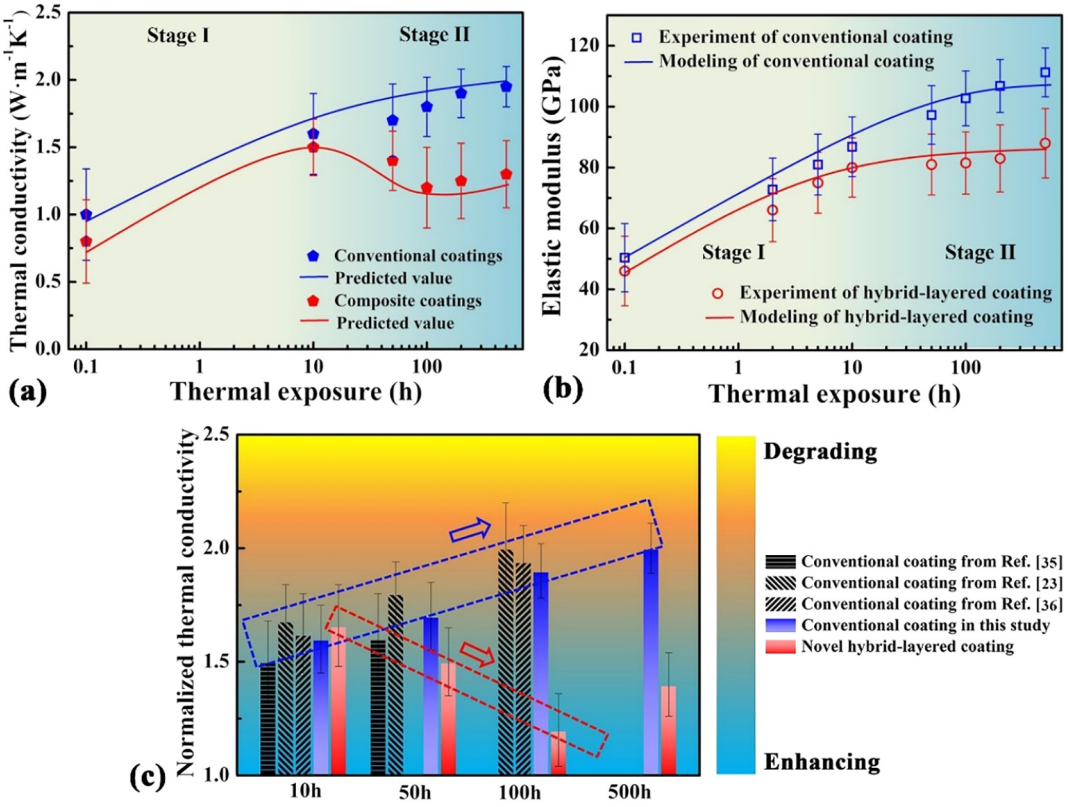

Fig. 8. Comparison between predicted values and experimental data: (a) thermal conductivity, (b) elastic modulus in microscale, (c) normalized thermal conductivity.

the hybrid-layered coatings is observed, whereas a slow increase is observed in the case of the conventional coatings. Overall, the newly formed pores enable the hybrid-layered coatings to undergo a self-decrease in thermal conductivity, which suggests that the novel hybrid-layered TBC structure offers a positive transformation of the sintering effect.

3.3. Correlation between microstructure and thermal/mechanical properties

Similar stage-sensitive evolutionary trends are clearly observed both in the properties and the microstructures, suggesting that the changes in the properties are highly associated with the redistribution of the 2D pores. Fig. 8 compares the predicted thermal/mechanical properties with experimental data. It is observed that the predicted values are consistent with the experimental values. Overall, the thermal durations are divided into two stages: a significantly faster and greater increase in the properties is observed during stage I, and the increase is caused by the decrease in the 2D micropore density. Subsequently, self-enhanced thermal insulation is observed during stage II, owing to the formation of 2D mesopores, as shown in Fig. 8c. In summary, the correlation between the microstructure and thermal/mechanical properties suggests that the changes in 2D pore densities in multiple scales predominantly determine the properties of the TBCs, which is consistent with the previous reports [28,56]. The mechanisms of 2D micropore healing and 2D mesopore formation, as well as the way they affect the properties, are discussed in the following sections.

4. Discussion

4.1. Scale-progressive healing mechanism of 2D micropores during stage I

In the as-deposited state, the 2D micropores play a dominant role in thermal insulation, because most of their orientations are perpendicular to the heat flux. However, these pores also bring the whole system to a higher free energy state. During thermal exposure, thermally activated matter is spontaneously transferred to decrease the free energy of the

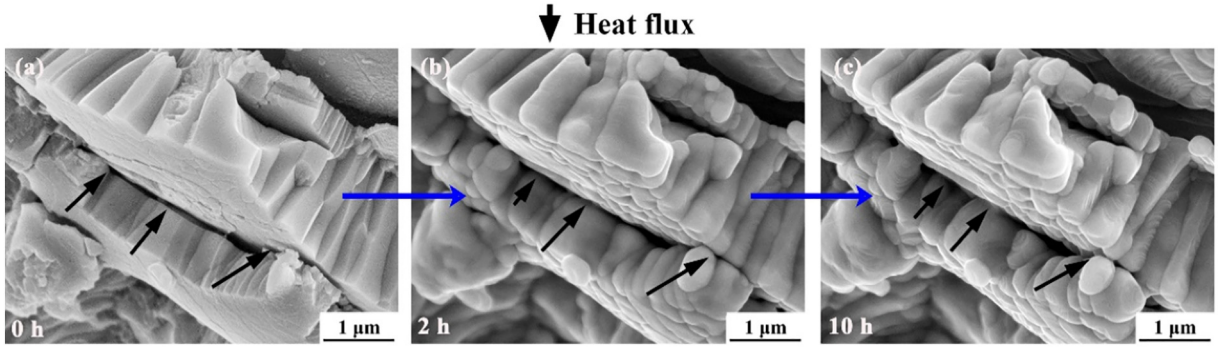

Fig. 9. In-situ healing process of a micropore observed from a fractured cross-section by SEM at: (a) 0 h, (b) 2 h, and (c) 10 h. The healing pore is highlighted by black arrows.

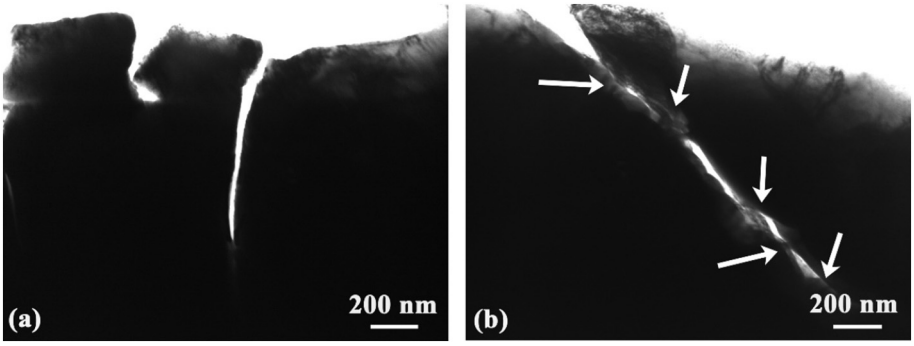

Fig. 10. Healing process of a micropore observed by TEM: (a) as-deposited state, and (b) state after thermal exposure for 5 h.

whole system, which is a common phenomenon in porous ceramic materials [57–59]. Regarding the PS-TBCs, the sintering-induced healing process is much more structure-specific due to the unique process through which matter transfer occurs. Generally, sintering begins from the contact area and proceeds by its extension; for example, the sintering of ceramic powders occurs when a contacting neck is formed between two powders [57]. Subsequently, the diameter of the neck gradually increases. Following this typical sintering mechanism, Cipitria et al. [19,60] investigated the sintering process of the PS-TBCs in a layer-stacking model. The model described the healing process of the 2D micropores as the increase in the diameter of the single contact region between the layers. The predicted results are well consistent with the experimental data during the entire thermal exposure process. However, the model could not explain the ultrafast kinetics during the initial stage (referred to as stage I in this study), although the increase in the properties mostly occurs at this stage. This suggests that the healing of 2D micropores during stage I should proceed in a different way. Figs. 9 and 10 show the healing process of a 2D micropore characterized by SEM and TEM, respectively. An obvious phenomenon is that the pore is bridge-connected at multiple points at the pore tips. As a result, a continuous pore is divided into several parts. This phenomenon has also been reported in previous studies [44,61]. The bridge connection at multiple points enables matter transfer through multiple paths, including the initial bonding area. This is different from the traditional understanding of the sintering process of porous materials [57]. Consequently, the sintering kinetics of the PS-TBCs are much higher during stage I. On the contrary, during stage II, the residual gap in the 2D micropores hinders multiple contacts between the counter surfaces; and as a result, the sintering kinetics significantly slow down. Furthermore, during the evolution of the lamellar TBCs prepared by plasma spraying, the variations in sintering kinetics are commonly known to be sensitive to the stage of the process [23–25,27]. The ultrafast increase in thermal conductivity and elastic modulus are the main causes for the degradation and failure of the TBCs after thermal exposure [40,62]. Therefore, understanding the mechanism of multiple contacts is critical for realizing a degradation-resistant design.

The multiple contacts of the 2D micropores are actually caused by sintering-induced material change and the morphology of these pores. Regarding the sintering-induced material change, it is easy to observe that roughening occurs at the surface of the splat (Fig. 9). This roughening phenomenon is also observed in other materials, e.g., $La_2Zr_2O_7$ [44]. Fig. 11 shows a quasi in-situ observation of pore surface by AFM [63]. The initial flat surface is observed to become uneven after thermal exposure. The degree of roughening appears to extend to multiple orders of

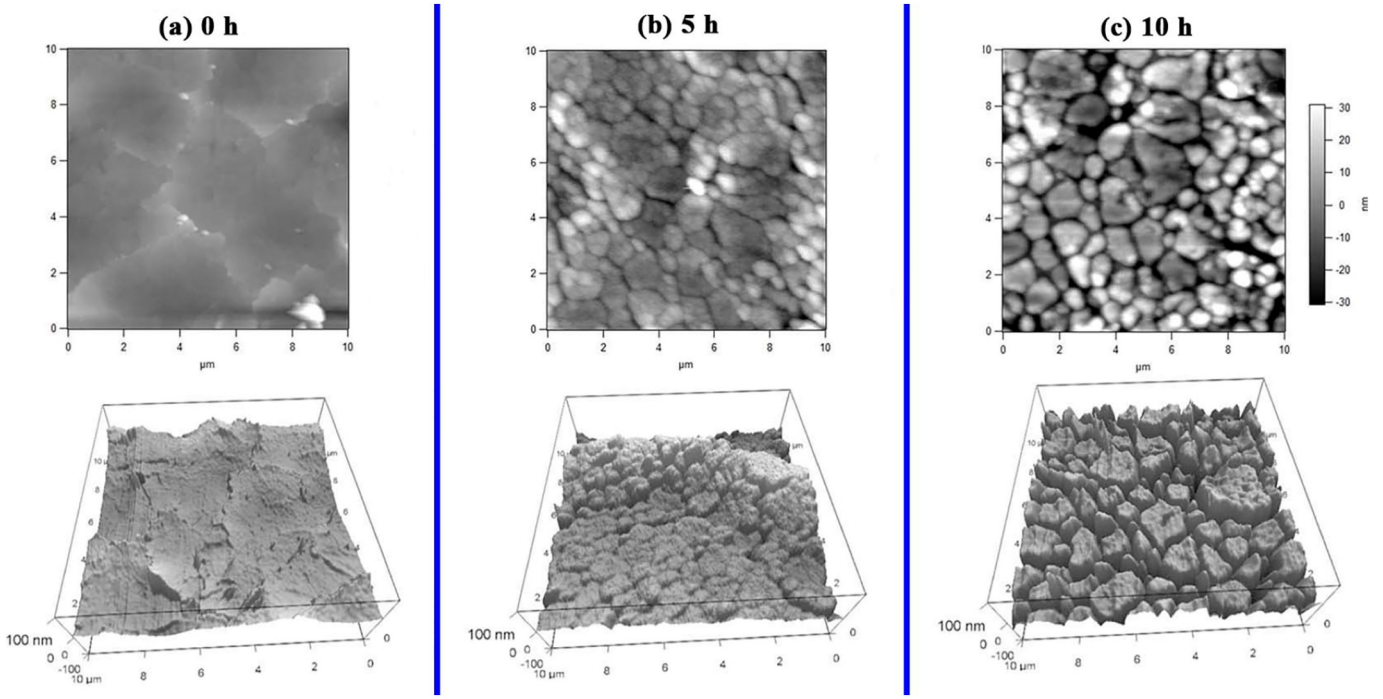

Fig. 11. In-situ observation of pore surface by AFM: (a) 0 h, (b) 5 h, and (c) 10 h [63].

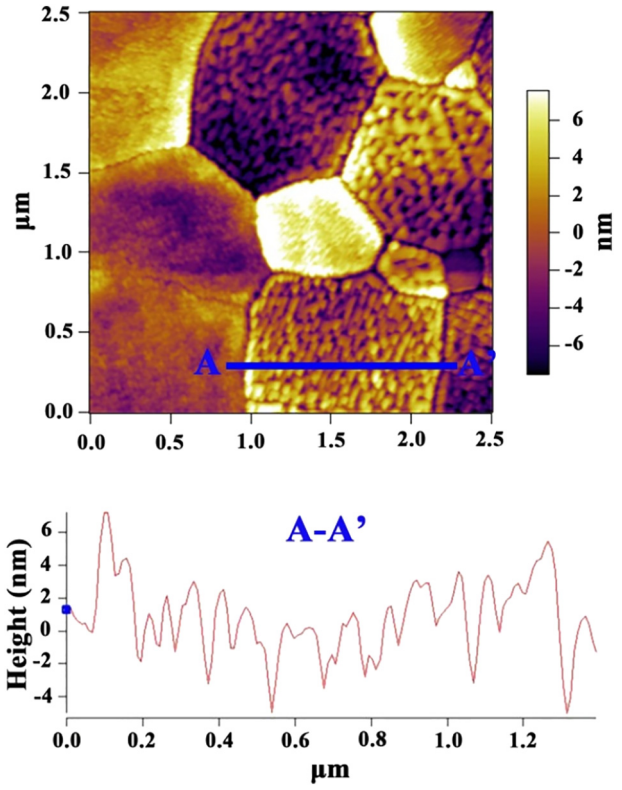

Fig. 12. Grain boundary grooving and surface faceting caused by thermal exposure.

magnitude, i.e., from several nanometers to tens of nanometers. This is caused by the special microstructure of the splats, which are formed by some columnar grains that are oriented parallelly to the heat flux. During plasma spraying, when molten droplets impact on the substrate or the predeposition, the grains nucleate and then rapidly grow into the residual molten parts along the direction of the deposition [64]. During thermal exposure, the boundaries between the columnar grains and the free surfaces (corresponding to the pore surface) would be the high-energy defects that need to be changed [65], as shown in Fig. 12. On the one hand, grain boundary grooving occurs between the grains and is driven by the grain boundary energy; and depending on the temperature (from 1000 to 1300 °C), matter transfer can change from being surface-diffusion dominant to volume-diffusion dominant [66]. On the other hand, surface faceting occurs at the free surface of the columnar grains, which is driven by the anisotropy of the free energy of the specific surface. Our previous report suggested that the degree of roughening of grain boundary grooving can be as high as 30 nm, whereas the surface faceting is approximately 5–10 nm [65,67]. In brief, during thermal exposure, the initially smooth pore surface becomes rough due to matter transfer between and inside the columnar grains.

Regarding the morphology of the 2D micropores, their width seems to be unequal; at the pore tips, the width is very narrow (often <10 nm). The abovementioned degree of roughening would possibly lead to contact between the counter surfaces at the pore tips. Since the width (~100 nm) is larger than the degree of roughening, there will be no bridge connection at the center of the pores. This can be essentially responsible for the stage-sensitive healing kinetics of the 2D micropores.

4.2. Self-enhancing mechanism of newly formed 2D mesopores during stage II

During stage II, the formation of new 2D mesopores results from the reversed and differential evolution of the dense splats and the nanoheaps [68,69]. The stacking of the dense splats forms a hybrid-layered structure of solid (splats) and gas (pores), whereas the nanoheaps are loose porous structures. During thermal exposure, both the hybrid-layered structure and the nanoheaps contract due to sintering. However, the degree of contraction of the nanoheaps is larger than that of the lamellar zones, owing to their loose structures [70]. In addition, the direction of the contraction may be opposite, and consequently, an interfacial opening occurs between the hybrid-layered structure and the nanoheaps, as shown in Fig. 13. This mechanism is similar to that in the PS nanostructured TBCs [71–73]. It is reported that the pores that are perpendicular to the heat flux would exhibit the strongest thermal barrier performance [28,49], since the route of heat flux is disturbed by introducing a very large thermal resistance. Therefore, it would be important that the newly formed pores should be perpendicular to the heat flux. In this study, the newly formed mesopores are actually the opening up of interface between the dense splats and nanoheaps. During the deposition, the dense splat and nanoheaps are both flatten perpendicular to the heat flux by and large. Therefore, this method enables the orientations of the newly formed 2D mesopores to be perpendicular to the heat flux, as shown in Fig. 5g, h. This would make a significant contribution to the thermal barrier performance.

Fig. 14 shows the morphologies of an individual micropore and mesopore, as well as their aspect ratios. It is observed that the width of the micropore gap is unequal, as discussed at the end of Section 4.1. In addition, the aspect ratios of the 2D micropores at the as-deposited state are in a range of 10–30, whereas those of the newly formed 2D

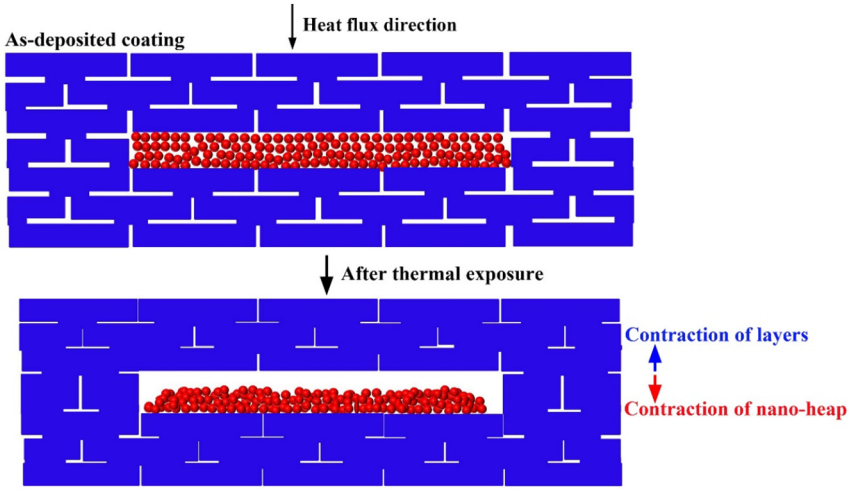

Fig. 13. Schematic showing the interfacial opening between the dense splats and a nanoheap.

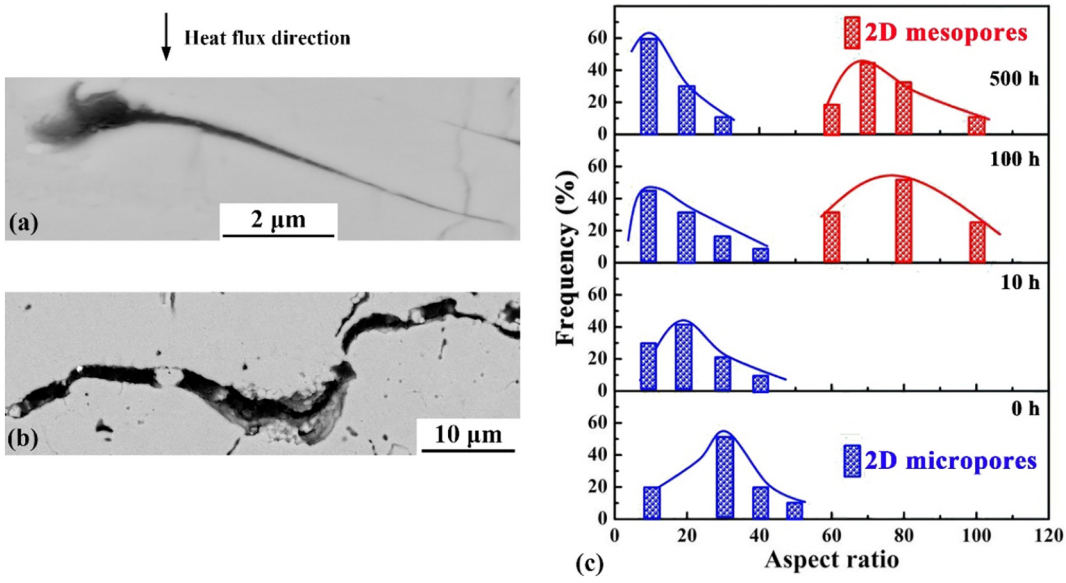

Fig. 14. Morphologies and aspect ratios of the 2D micropores and the 2D mesopores: (a) morphology of an individual 2D micropore, (b) morphology of an individual 2D mesopore, (c) aspect ratios of the 2D micropores and the 2D mesopores.

mesopores are approximately 60–100. Given the changes in the 2D pore length density (Fig. 6) and aspect ratio (Fig. 14), it can be concluded that 2D micropores with smaller aspect ratios disappeared during stage I, while some 2D mesopores with larger aspect ratios were formed during stage II.

Fig. 15 shows the effect of aspect ratio on the temperature distribution and heat flux in a hybrid-layered structure. Obviously, a higher aspect ratio leads to a greater temperature drop. Moreover, the pores result in a 2D distribution of heat flux, particularly at the pore tips. This means that the heat flux at the pore tips would deviate from the original path, since the solid has a significantly higher thermal conductivity than that of the air-entrapped pores. As a result, for a single pore, the heat flux would pass through the pore center (defined as the effective area), whereas the heat flux would bypass the pore tips (defined as the ineffective area). This phenomenon can also be found in other reports [74,75]. The final thermal insulation of a pore would thereby be dominantly determined by the ratio of the effective area with respect to the total area.

Fig. 16 shows the ratio of the effective area with respect to the total area as a function of the aspect ratio of the pores. The critical area is determined by a critical condition shown in Eq. (9) [49]:

$$|q_x| = |q_y| \tag{9}$$

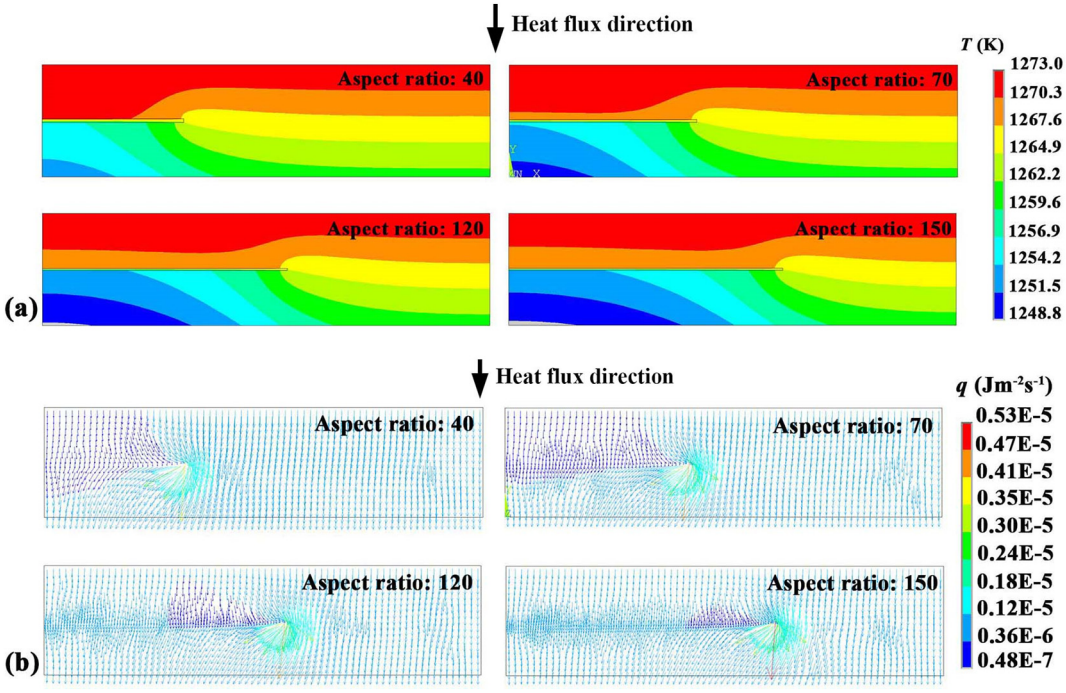

Fig. 15. Effect of aspect ratio on (a) temperature distribution, and (b) heat flux.

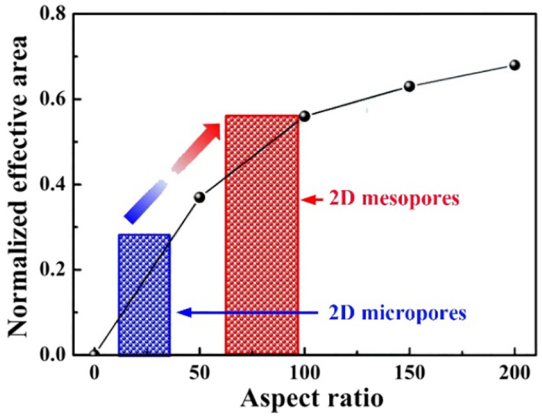

Fig. 16. Ratios of the effective area with respect to the total area as a function of the aspect ratio of the pores.

where q_x is the x-component of the heat flux, and q_y is the y-component of the heat flux.

It is observed that the ratio of the effective area of the 2D pores increases with the increase in their aspect ratios. Moreover, the increase is significantly faster in the aspect ratio range of 0–100. The aspect ratio of the 2D micropores is approximately 10–30 [11,13,16,24,54]; correspondingly, the ratio of the effective area to hinder heat is <40%. In contrast, the aspect ratio of the newly formed 2D mesopores is approximately 60–100, which increases their ratios of effective area to approximately 60%. This is the reason for the decrease in the thermal conductivity when the 2D mesopores are formed. Furthermore, the newly formed 2D mesopores often have a larger width (>50 nm). Based on the discussion in Section 4.1, these pores would have a very low healing rate, since no multiple contact occurs. Therefore, consistently high thermal insulation can be expected during a long thermal exposure. In brief, the novel hybrid-layered structure produces some new pores with more effective area to prevent heat flux, albeit at the price of the 2D micropores with limited function to hinder heat flux. This structural design enables a self-enhancing thermal barrier function during thermal exposure.

However, it is worth noting that these 2D mesopores may have a negative effect on the lifetime of the TBCs. During real service, the TBCs are often under a stressed state (e.g., thermal expansion mismatch stress between the coating and substrate), and the newly formed pores with larger scale may increase the possibility of spallation. This study mainly focuses on the structural design to achieve a self-enhancing thermal barrier performance. The combined effect of the newly formed pores on the lifetime and thermal insulation of the TBCs should be investigated further to optimize the structure such that it provides high thermal insulation as well as long lifetime.

5. Conclusions

Novel hybrid-layered TBCs are designed and prepared using a co-spraying method. The evolution of the microstructures and their properties during thermal exposure were investigated from the perspective of the healing of 2D micropores and the formation of 2D mesopores; and the underlying mechanisms responsible for the degradation-resistant behavior were investigated. The detailed conclusions are as follows:

(i) The hybrid-layered TBCs were formed by the alternate stacking of dense splats and porous nanoheaps. Thermal exposure leads to significant two-stage evolution trends of thermal and mechanical properties. During stage I, the thermal conductivity is increased by 60%. In contrast, during stage II, the thermal conductivity is decreased by 25%. Compared to the conventional TBCs, the novel hybrid-layered TBCs exhibit a 50% self-enhancement of thermal barrier performance.

(ii) The 2D pores perpendicular to the heat flux dominantly determine the thermal properties of the TBCs. During stage I, the ultrafast healing of the 2D micropores is attributed primarily to the multiple contacts caused by multiscale roughening. During stage II, some new 2D mesopores are formed at the interface of the dense splats and nanoheaps. Compared to the 2D micropores, the newly formed 2D mesopores have a much larger aspect ratio, which increases the ratio of the effective area to prevent heat flux from 30% to 60%, which is primarily responsible for the self-enhancement of the thermal properties.

The novel hybrid-layered structure provides a feasible means for the TBCs to work against the degradation caused by sintering, which is the main objective of the advanced TBCs that can be used in next generation applications.

CRediT authorship contribution statement

Guang-Rong Li: Writing - original draft. **Li-Shuang Wang:** Software. **Guan-Jun Yang:** Supervision.

Acknowledgments

This work was supported by the National Natural Science Foundation of China (grant number 51801148); the China Postdoctoral Science Foundation (grant number 2018M631151); the Equipment Advance Research Foundation of China (grant number 61409220117); the Shaanxi Province Postdoctoral Science Foundation; the Fundamental Research Funds for the Central Universities; and the National Program for Support of Top-notch Young Professionals.

Declarations of interest

None.

Data availability

The raw/processed data required to reproduce these findings cannot be shared at this time as the data also forms part of an ongoing study.

Individual contribution of each author

G.-J. Yang designed and supervised the project, G.-R. Li carried out the experiments and wrote the paper, L.-S. Wang performed the calculations. All the authors contributed to the discussion.

References

[1] N.P. Padture, M. Gell, E.H. Jordan, Materials science - thermal barrier coatings for gas-turbine engine applications, Science 296 (5566) (2002) 280–284.
[2] N.P. Padture, Advanced structural ceramics in aerospace propulsion, Nat. Mater. 15 (8) (2016) 804–809.
[3] W. Zhu, Z.B. Zhang, L. Yang, Y.C. Zhou, Y.G. Wei, Spallation of thermal barrier coatings with real thermally grown oxide morphology under thermal stress, Mater. Des. 146 (2018) 180–193.
[4] A. Ganvir, S. Joshi, N. Markocsan, R. Vassen, Tailoring columnar microstructure of axial suspension plasma sprayed TBCs for superior thermal shock performance, Mater. Des. 144 (2018) 192–208.
[5] F. Nozahic, C. Estournes, A.L. Carabat, W.G. Sloof, S. van der Zwaag, D. Monceau, Self-healing thermal barrier coating systems fabricated by spark plasma sintering, Mater. Des. 143 (2018) 204–213.
[6] J. Krishnasamy, S.A. Ponnusami, S. Turteltaub, S. van der Zwaag, Modelling the fracture behaviour of thermal barrier coatings containing healing particles, Mater. Des. 157 (2018) 75–86.
[7] Y.Z. Liu, X.B. Hu, S.J. Zheng, Y.L. Zhu, H. Wei, X.L. Ma, Microstructural evolution of the interface between NiCrAlY coating and superalloy during isothermal oxidation, Mater. Des. 80 (2015) 63–69.
[8] Z.L. Qu, K. Wei, Q. He, R.J. He, Y.M. Pei, S.X. Wang, D.N. Fang, High temperature fracture toughness and residual stress in thermal barrier coatings evaluated by an in-situ indentation method, Ceram. Int. 44 (7) (2018) 7926–7929.

[9] P. Jiang, X.L. Fan, Y.L. Sun, D.J. Li, T.J. Wang, Bending-driven failure mechanism and modelling of double-ceramic-layer thermal barrier coating system, Int. J. Solids Struct. 130 (2018) 11–20.
[10] D.R. Clarke, M. Oechsner, N.P. Padture, Thermal-barrier coatings for more efficient gas-turbine engines, MRS Bull. 37 (10) (2012) 891–902.
[11] R. Vassen, A. Stuke, D. Stover, Recent developments in the field of thermal barrier coatings, J. Therm. Spray Technol. 18 (2) (2009) 181–186.
[12] E. Bakan, R. Vassen, Ceramic top coats of plasma-sprayed thermal barrier coatings: materials, processes, and properties, J. Therm. Spray Technol. 26 (6) (2017) 992–1010.
[13] S. Sampath, U. Schulz, M.O. Jarligo, S. Kuroda, Processing science of advanced thermal-barrier systems, MRS Bull. 37 (10) (2012) 903–910.
[14] G. Mauer, R. Vassen, Current developments and challenges in thermal barrier coatings, Surf. Eng. 27 (7) (2011) 477–479.
[15] W.G. Chi, S. Sampath, H. Wang, Microstructure-thermal conductivity relationships for plasma-sprayed yttria-stabilized zirconia coatings, J. Am. Ceram. Soc. 91 (8) (2008) 2636–2645.
[16] E. Bakan, D.E. Mack, G. Mauer, R. Mucke, R. Vassen, Porosity-property relationships of plasma-sprayed $Gd_2Zr_2O_7$/YSZ thermal barrier coatings, J. Am. Ceram. Soc. 98 (8) (2015) 2647–2654.
[17] S. Kyaw, A. Jones, M.A.E. Jepson, T. Hyde, R.C. Thomson, Effects of three-dimensional coating interfaces on thermo-mechanical stresses within plasma spray thermal barrier coatings, Mater. Des. 125 (2017) 189–204.
[18] J. Sun, Q.G. Fu, R.M. Yuan, K.Y. Dong, J.J. Guo, Corrosion and thermal cycling behavior of plasma sprayed thermal barrier coatings on die steel, Mater. Des. 114 (2017) 537–545.
[19] A. Cipitria, I.O. Golosnoy, T.W. Clyne, A sintering model for plasma-sprayed zirconia TBCs. Part I: free-standing coatings, Acta Mater. 57 (4) (2009) 980–992.
[20] F. Fanicchia, X. Maeder, J. Ast, A.A. Taylor, Y. Guo, M.N. Polyakov, J. Michler, D.A. Axinte, Residual stress and adhesion of thermal spray coatings: microscopic view by solidification and crystallisation analysis in the epitaxial CoNiCrAlY single splat, Mater. Des. 153 (2018) 36–46.
[21] X.T. Luo, M.L. Yao, N. Ma, M. Takahashi, C.J. Li, Deposition behavior, microstructure and mechanical properties of an in-situ micro-forging assisted cold spray enabled additively manufactured Inconel 718 alloy, Mater. Des. 155 (2018) 384–395.
[22] X.T. Luo, C.J. Li, Tailoring the composite interface at lower temperature by the nanoscale interfacial active layer formed in cold sprayed cBN/NiCrAl nanocomposite, Mater. Des. 140 (2018) 387–399.
[23] F. Cernuschi, P.G. Bison, S. Marinetti, P. Scardi, Thermophysical, mechanical and microstructural characterization of aged free-standing plasma-sprayed zirconia coatings, Acta Mater. 56 (16) (2008) 4477–4488.
[24] S. Paul, A. Cipitria, S.A. Tsipas, T.W. Clyne, Sintering characteristics of plasma sprayed zirconia coatings containing different stabilisers, Surf. Coat. Technol. 203 (8) (2009) 1069–1074.
[25] Y. Tan, J.P. Longtin, S. Sampath, H. Wang, Effect of the starting microstructure on the thermal properties of as-sprayed and thermally exposed plasma-sprayed YSZ coatings, J. Am. Ceram. Soc. 92 (3) (2009) 710–716.
[26] R. Vassen, N. Czech, W. Mallener, W. Stamm, D. Stover, Influence of impurity content and porosity of plasma-sprayed yttria-stabilized zirconia layers on the sintering behaviour, Surf. Coat. Technol. 141 (2–3) (2001) 135–140.
[27] J.A. Thompson, T.W. Clyne, The effect of heat treatment on the stiffness of zirconia top coats in plasma-sprayed TBCs, Acta Mater. 49 (9) (2001) 1565–1575.
[28] Z. Wang, A. Kulkarni, S. Deshpande, T. Nakamura, H. Herman, Effects of pores and interfaces on effective properties of plasma sprayed zirconia coatings, Acta Mater. 51 (18) (2003) 5319–5334.
[29] D.R. Clarke, Materials selection guidelines for low thermal conductivity thermal barrier coatings, Surf. Coat. Technol. 163 (2003) 67–74.
[30] X.J. Lu, P. Xiao, Constrained sintering of YSZ/Al_2O_3 composite coatings on metal substrates produced from eletrophoretic deposition, J. Eur. Ceram. Soc. 27 (7) (2007) 2613–2621.
[31] B. Ercan, K.J. Bowman, R.W. Trice, H. Wang, W. Porter, Effect of initial powder morphology on thermal and mechanical properties of stand-alone plasma-sprayed 7 wt. % Y_2O_3-ZrO_2 coatings, Mater. Sci. Eng. A 435 (2006) 212–220.
[32] L. Xie, M.R. Dorfman, A. Cipitria, S. Paul, I.O. Golosnoy, T.W. Clyne, Properties and performance of high-purity thermal barrier coatings, J. Therm. Spray Technol. 16 (5–6) (2007) 804–808.
[33] X.G. Chen, H.M. Zhang, H.S. Zhang, Y.D. Zhao, G. Li, $Ce_{1-x}Sm_xO_{2-x/2}$—a novel type of ceramic material for thermal barrier coatings, J. Adv. Ceram. 5 (3) (2016) 244–252.
[34] B.R. Marple, R.S. Lima, C. Moreau, S.E. Kruger, L. Xie, M.R. Dorfman, Yttria-stabilized zirconia thermal barriers sprayed using N_2-H_2 and Ar-H_2 plasmas: influence of processing and heat treatment on coating properties, J. Therm. Spray Technol. 16 (5–6) (2007) 791–797.
[35] R. Dutton, R. Wheeler, K.S. Ravichandran, K. An, Effect of heat treatment on the thermal conductivity of plasma-sprayed thermal barrier coatings, J. Therm. Spray Technol. 9 (2) (2000) 204–209.
[36] F. Cernuschi, L. Lorenzoni, S. Ahmaniemi, P. Vuoristo, T. Mantyla, Studies of the sintering kinetics of thick thermal barrier coatings by thermal diffusivity measurements, J. Eur. Ceram. Soc. 25 (4) (2005) 393–400.
[37] D.M. Zhu, R.A. Miller, Thermal conductivity and elastic modulus evolution of thermal barrier coatings under high heat flux conditions, J. Therm. Spray Technol. 9 (2) (2000) 175–180.
[38] G.J. Yang, Z.L. Chen, C.X. Li, C.J. Li, Microstructural and mechanical property evolutions of plasma-sprayed YSZ coating during high-temperature exposure: comparison study between 8YSZ and 20YSZ, J. Therm. Spray Technol. 22 (8) (2013) 1294–1302.
[39] S.R. Choi, D.M. Zhu, R.A. Miller, Effect of sintering on mechanical properties of plasma-sprayed zirconia-based thermal barrier coatings, J. Am. Ceram. Soc. 88 (10) (2005) 2859–2867.
[40] M. Shinozaki, T.W. Clyne, A methodology, based on sintering-induced stiffening, for prediction of the spallation lifetime of plasma-sprayed coatings, Acta Mater. 61 (2) (2013) 579–588.
[41] G.R. Li, H. Xie, G.J. Yang, G. Liu, C.X. Li, C.J. Li, A comprehensive sintering mechanism for TBCs-part I: an overall evolution with two-stage kinetics, J. Am. Ceram. Soc. 100 (5) (2017) 2176–2189.
[42] P. Jiang, X.L. Fan, Y.L. Sun, D.J. Li, B. Li, T.J. Wang, Competition mechanism of interfacial cracks in thermal barrier coating system, Mater. Des. 132 (2017) 559–566.
[43] S. Kikuchi, M. Tezura, M. Kimura, N. Yamaguchi, S. Kitaoka, T. Kizuka, In situ transmission electron microscopy of high-temperature degradation of yttria-stabilized zirconia thermal barrier coatings, Scr. Mater. 150 (2018) 50–53.
[44] T. Liu, X.T. Luo, X. Chen, G.J. Yang, C.X. Li, C.J. Li, Morphology and size evolution of interlamellar two-dimensional pores in plasma-sprayed $La_2Zr_2O_7$ coatings during thermal exposure at 1300 °C, J. Therm. Spray Technol. 24 (5) (2015) 739–748.
[45] T. Liu, S.L. Zhang, X.T. Luo, G.J. Yang, C.X. Li, C.J. Li, High heat insulating thermal barrier coating designed with large two-dimensional inter-lamellar pores, J. Therm. Spray Technol. 25 (1–2) (2016) 222–230.
[46] Y. Yang, Y.F. Cheng, Bi-layered CeO_2/$SrTiO_3$ nanocomposite photoelectrode for energy storage and photocathodic protection, Electrochim. Acta 253 (2017) 134–141.
[47] N. Zidane, Y.A. Albrimi, A.A. Addi, J. Douch, R.M. Souto, M. Hamdani, Evaluation of the corrosion of AZ31 magnesium alloy used as sacrificial anode for cathodic protection of hot-water tank storage containing chloride, Int. J. Electrochem. Sci. 13 (1) (2018) 29–44.
[48] A. Osundare, D.T. Oloruntoba, P. Popoola, Development of carbon anode for cathodic protection of mild steel in chloride environment, Anti-Corros. Methods Mater. 65 (2) (2018) 158–165.
[49] W.W. Zhang, G.R. Li, Q. Zhang, G.J. Yang, Multiscale pores in TBCs for lower thermal conductivity, J. Therm. Spray Technol. 26 (6) (2017) 1183–1197.
[50] W.W. Zhang, G.R. Li, Q. Zhang, G.J. Yang, G.W. Zhang, H.M. Mu, Bimodal TBCs with low thermal conductivity deposited by a powder-suspension co-spray process, J. Mater. Sci. Technol. 34 (8) (2018) 1293–1304.
[51] R. Vassen, Y. Kagawa, R. Subramanian, P. Zombo, D.M. Zhu, Testing and evaluation of thermal-barrier coatings, MRS Bull. 37 (10) (2012) 911–916.
[52] G.R. Li, G.J. Yang, C.X. Li, C.J. Li, Strain-induced multiscale structural changes in lamellar thermal barrier coatings, Ceram. Int. 43 (2) (2017) 2252–2266.
[53] H.J. Ratzer-Scheibe, U. Schulz, The effects of heat treatment and gas atmosphere on the thermal conductivity of APS and EB-PVD PYSZ thermal barrier coatings, Surf. Coat. Technol. 201 (18) (2007) 7880–7888.
[54] G.R. Li, B.W. Lv, G.J. Yang, W.X. Zhang, C.X. Li, C.J. Li, Relationship between lamellar structure and elastic modulus of thermally sprayed thermal barrier coatings with intra-splat cracks, J. Therm. Spray Technol. 24 (8) (2015) 1355–1367.
[55] W.X. Zhang, T.J. Wang, L.X. Li, Numerical analysis of the transverse strengthening behavior of fiber-reinforced metal matrix composites, Comput. Mater. Sci. 39 (3) (2007) 684–696.
[56] G.R. Li, G.J. Yang, C.X. Li, C.J. Li, A comprehensive sintering mechanism for thermal barrier coatings-part III: substrate constraint effect on healing of 2D pores, J. Am. Ceram. Soc. 101 (8) (2018) 3636–3648.
[57] A.J. Shaler, H. Udin, G.C. Kuczynski, M. Bever, Self-diffusion in sintering of metallic particles - discussion, Trans. AIME 185 (11) (1949) 896–897.
[58] A.N. Chen, M. Li, J. Xu, C.H. Lou, J.M. Wu, L.J. Cheng, Y.S. Shi, C.H. Li, High-porosity mullite ceramic foams prepared by selective laser sintering using fly ash hollow spheres as raw materials, J. Eur. Ceram. Soc. 38 (13) (2018) 4553–4559.
[59] F.C. Cao, X.H. Fan, B. Liu, X.F. Zhao, F.W. Guo, P. Xiao, Microstructure and thermal conductivity of fully ceramic microencapsulated fuel fabricated by spark plasma sintering, J. Am. Ceram. Soc. 101 (9) (2018) 4224–4236.
[60] A. Cipitria, I.O. Golosnoy, T.W. Clyne, A sintering model for plasma-sprayed zirconia thermal barrier coatings. Part II: coatings bonded to a rigid substrate, Acta Mater. 57 (4) (2009) 993–1003.
[61] B. Lv, X. Fan, H. Xie, T.J. Wang, Effect of neck formation on the sintering of air-plasma-sprayed thermal barrier coating system, J. Eur. Ceram. Soc. 37 (2) (2017) 811–821.
[62] B. Cheng, G.J. Yang, Q. Zhang, N. Yang, M. Zhang, Y.M. Zhang, C.X. Li, C.J. Li, Gradient thermal cyclic behaviour of $La_2Zr_2O_7$/YSZ DCL-TBCs with equivalent thermal insulation performance, J. Eur. Ceram. Soc. 38 (4) (2018) 1888–1896.
[63] G.R. Li, H. Xie, G.J. Yang, Scale-progressive healing mechanism dominating the ultrafast initial sintering kinetics of plasma-sprayed thermal barrier coatings, Ceram. Int. 44 (14) (2018) 16732–16738.
[64] R. McPherson, On the formation of thermally sprayed alumina coatings, J. Mater. Sci. 15 (12) (1980) 3141–3149.
[65] G.R. Li, H. Xie, G.J. Yang, G. Liu, C.X. Li, C.J. Li, A comprehensive sintering mechanism for TBCs-part II: multiscale multipoint interconnection-enhanced initial kinetics, J. Am. Ceram. Soc. 100 (9) (2017) 4240–4251.
[66] K.A. Erk, C. Deschaseaux, R.W. Trice, Grain-boundary grooving of plasma-sprayed yttria-stabilized zirconia thermal barrier coatings, J. Am. Ceram. Soc. 89 (5) (2006) 1673–1678.
[67] G.R. Li, G.J. Yang, C.X. Li, C.J. Li, A comprehensive mechanism for the sintering of plasma-sprayed nanostructured thermal barrier coatings, Ceram. Int. 43 (13) (2017) 9600–9615.
[68] N. Wang, C.N. Zhou, S.K. Gong, H.B. Xu, Heat treatment of nanostructured thermal barrier coating, Ceram. Int. 33 (6) (2007) 1075–1081.
[69] R.S. Lima, A. Kucuk, C.C. Berndt, Bimodal distribution of mechanical properties on plasma sprayed nanostructured partially stabilized zirconia, Mater. Sci. Eng. A 327 (2) (2002) 224–232.
[70] M. Gell, Application opportunities for nanostructured materials and coatings, Mater. Sci. Eng. A 204 (1–2) (1995) 246–251.

[71] H.Q. Lavasani, Z. Valefi, N. Ehsani, S.T. Masoule, Comparison of the effect of sintering on the microstructure, micro hardness and phase composition of conventional and nanostructured YSZ TBCs, Ceram. Int. 43 (15) (2017) 12497–12504.
[72] R.S. Lima, B.R. Marple, Nanostructured YSZ thermal barrier coatings engineered to counteract sintering effects, Mater. Sci. Eng. A 485 (1–2) (2008) 182–193.
[73] G.R. Li, G.J. Yang, C.X. Li, C.J. Li, Stage-sensitive microstructural evolution of nanostructured TBCs during thermal exposure, J. Eur. Ceram. Soc. 38 (9) (2018) 3325–3332.
[74] I.O. Golosnoy, S.A. Tsipas, T.W. Clyne, An analytical model for simulation of heat flow in plasma-sprayed thermal barrier coatings, J. Therm. Spray Technol. 14 (2) (2005) 205–214.
[75] I.O. Golosnoy, A. Cipitria, T.W. Clyne, Heat transfer through plasma-sprayed thermal barrier coatings in gas turbines: a review of recent work, J. Therm. Spray Technol. 18 (5–6) (2009) 809–821.